



A bottom-up building process of nanostructured $\text{La}_{0.75}\text{Sr}_{0.25}\text{Cr}_{0.5}\text{Mn}_{0.5}\text{O}_{3-\delta}$ electrodes for symmetrical-solid oxide fuel cell: Synthesis, characterization and electrocatalytic testing

Corina M. Chanquía ^{a,b,*}, Alejandra Montenegro-Hernández ^{a,b}, Horacio E. Troiani ^{a,b}, Alberto Caneiro ^{a,b}

^a Centro Atómico Bariloche, Comisión Nacional de Energía Atómica, Av. Ezequiel Bustillo 9500, R8402AGP San Carlos de Bariloche, Río Negro, Argentina
^b CONICET, Avenida Rivadavia 1917, C1033AAJ Buenos Aires, Argentina



HIGHLIGHTS

- Pure-phase LSCM nanopowder has been successfully synthesized by combustion method.
- A detailed morphological, textural and structural characterization is presented.
- A bottom-up building process of LSCM nanoelectrodes onto LSGM electrolyte was performed.
- Electrocatalytic responses of the cells, under oxidizing and reducing atmospheres, are discussed.
- The ASR trends obtained were correlated with the electrode microstructure.

ARTICLE INFO

Article history:

Received 11 April 2013

Received in revised form

19 June 2013

Accepted 22 June 2013

Available online 4 July 2013

Keywords:

Perovskite oxide
 Combustion method
 Nanocrystallites
 Nanoelectrodes
 Symmetrical cells
 Solid oxide fuel cells

ABSTRACT

Pure-phase $\text{La}_{0.75}\text{Sr}_{0.25}\text{Cr}_{0.5}\text{Mn}_{0.5}\text{O}_{3-\delta}$ (LSCM) nanocrystallites have been successfully synthesized by the combustion method, employing glycine as fuel and complexing agent, and ammonium nitrate as combustion trigger. A detailed morphological and structural characterization is performed, by using of X-ray diffraction, N_2 physisorption and electron microscopy. The LSCM material consists in interconnected nanocrystallites (~ 30 nm) forming a sponge-like structure with meso and macropores, being its specific surface area around $10 \text{ m}^2 \text{ g}^{-1}$. Crystalline structural analyses show that the LSCM nanopowder has trigonal/rhombohedral symmetry in the $R-3c$ space group. By employing the spin coating technique and quick-stuck thermal treatments of the ink-electrolyte, electrodes with different crystallite size (95, 160 and 325 nm) are built onto both sides of the $\text{La}_{0.8}\text{Sr}_{0.2}\text{Ga}_{0.8}\text{Mg}_{0.2}\text{O}_{3-\delta}$ -disk electrolyte. To test the influence of the electrode crystallite size on the electrocatalytic behavior of the symmetrical cells, electrochemical impedance spectroscopy measurements at 800°C were performed. When the electrode crystallite size becomes smaller, the area specific resistance decreases from 3.6 to $1.31 \Omega \text{ cm}^2$ under $0.2\text{O}_2 - 0.8\text{Ar}$ atmosphere, possibly due to the enlarging of the triple-phase boundary, while this value increases from 7.04 to $13.78 \Omega \text{ cm}^2$ under $0.17\text{H}_2 - 0.03\text{H}_2\text{O} - 0.8\text{Ar}$ atmosphere, probably due to thermodynamic instability of the LSCM nanocrystallites.

© 2013 Elsevier B.V. All rights reserved.

1. Introduction

Solid oxide fuel cells (SOFCs) have attracted a great attention due to its high efficiency and the more clean electrical power

generation [1]. A SOFC device mainly consists of three components: a porous cathode, a porous anode and a dense electrolyte. The traditional materials used in SOFC operating between 800 and 1000°C are yttria-stabilized zirconia (YSZ) as electrolyte, Ni/YSZ cermet as anode and $\text{La}_{0.8}\text{Sr}_{0.2}\text{MnO}_3$ as cathode [2]. Strontium-substituted manganites have been chosen due to their excellent electronic conductivities and good catalytic behavior toward oxygen reduction [2]. Ni/YSZ offers excellent catalytic properties, electronic/ionic conductivity and good current collection. However, such cermets present some disadvantages

* Corresponding author. Centro Atómico Bariloche, Comisión Nacional de Energía Atómica, Av. Ezequiel Bustillo 9500, R8402AGP San Carlos de Bariloche, Río Negro, Argentina. Tel./fax: +54 294 4445288.

E-mail addresses: cchanquia@gmail.com, cchanquia@cab.cnea.gov.ar (C.M. Chanquía).

related to the low tolerance to sulfur and carbon built up when using hydrocarbon fuels [3–5].

Symmetrical-solid oxide fuel cells (S-SOFC), as an alternative approach to this configuration, adopt the same material both as anode and cathode, simultaneously. It has several advantages compared to the conventional SOFCs. The reduced number of cell components could facilitate the assembly of a fuel cell in a single thermal treatment and minimize compatibility requirements (thermal and chemical). Besides, this configuration could overcome two main drawbacks associated with SOFC technology when it directly operates with hydrocarbon fuels, i.e., the reversible sulfur poisoning and carbon deposition due to the possibility to revert the gas flow which will oxidize any sulfur species or carbon deposit [6,7]. The requirements for candidate symmetrical electrode materials are rather stringent, as they should include all the conditions applicable to an anode and cathode simultaneously: (1) good catalytic activity toward oxygen reduction and fuel oxidation; (2) chemical stability under both reducing and oxidizing atmospheres; (3) compatible thermal expansion with the other fuel cell components; and (4) acceptable electron and oxygen ion conductivity in both reducing and oxidizing atmospheres. Therefore, it is a challenging task to find materials that meet all requirements simultaneously. Thus, the typical performances obtained for S-SOFCs are somewhat lower as compared to traditional Fuel Cells due to the extreme difficulty to find a perfect material that fulfills all the requirements [8].

Up to now, only a very limited number of materials has been successfully demonstrated as electrodes of symmetrical-SOFCs [8–11]. A promising combination of properties, including phase and dimensional stability, high electrochemical activity in both reducing and oxidizing atmospheres, and chemical compatibility with various solid electrolytes, was recently reported for $(\text{La},\text{Sr})(\text{Cr},\text{Mn})\text{O}_{3-\delta}$ perovskites [12–19]. $\text{La}_{0.75}\text{Sr}_{0.25}\text{Cr}_{0.5}\text{Mn}_{0.5}\text{O}_{3-\delta}$ (LSCM) represents one of the most attractive materials [7,10,12,16,20,21]. The LSCM composition arises from the need to combine the properties of $\text{La}_{1-x}\text{A}_x\text{CrO}_{3\pm\delta}$ and $\text{La}_{1-x}\text{A}_x\text{MnO}_{3\pm\delta}$ materials. Chromite-based materials have been generally employed as interconnecting materials for SOFCs due to their relatively good stability in both reducing and oxidizing atmospheres at high temperatures [12,22]. The reported polarization resistance using these materials is too high for efficient SOFC operation, although significant improvements have been achieved by using doping in the B-site [12]. Manganite-based materials, as mentioned above, are the standard choice as cathode but they are unstable in anode conditions [7,23]. The main limitation to the LSCM material is its lower ionic conduction compared with the known mixed-conducting electrode materials and solid electrolytes [24].

The electrocatalytic performances of the anode and the cathode in SOFCs are critically dependent on the microstructures of the electrode layer, in particular, the total length of the triple-phase boundary (i.e. interface between electrolyte disk, electrode material and gas phase) and its porosity and tortuosity. These properties, in turn, are strongly dependent on the features of the starting oxide powder and its synthesis process [20]. In the literature, solid state reaction is the main synthesis process reported for type-perovskite LSCM oxides [6,12,17,18,25–30]. This synthesis route produces materials with large particle sizes ($>5\text{ }\mu\text{m}$) and low porosity, mainly due to the high synthesis temperature employed ($>1300\text{ }^{\circ}\text{C}$). Therefore, the preparation of fine and pure-phase LSCM powders with less agglomeration is desirable to improve the electrode performance.

In this context, the so-called combustion method has been considered as an attractive way to synthesize a wide variety of ultrafine particles of metallic oxides including perovskites [31,32]. This is a simple method with the advantage of using inexpensive

precursors and producing highly reactive nano-sized powders. The resulting powders are crystalline, homogeneous, softly agglomerated, and vary in size between 1 and 100 nm depending upon composition and synthesis parameters. This process is simple, rapid, low cost, and environmentally compatible [33]. However, the mechanism of the combustion reaction is quite complex because many parameters influence the reaction such as the chemical nature of the fuel molecule, the fuel to oxidizer ratio, the use of excess oxidizer, the use of combustion aid, the ignition temperature and the water content of the precursor mixture. In a previous work we reported the synthesis and characterization of pure-phase LSCM fine-crystallites showing a size distribution around 200 nm, which were prepared by the combustion method evaluating the influence of the glycine-to-nitrates molar ratio and the subsequent thermal treatment [34].

In the present study, the former aim is the optimization of the combustion synthesis conditions to obtain a pure-phase $\text{La}_{0.75}\text{Sr}_{0.25}\text{Cr}_{0.5}\text{Mn}_{0.5}\text{O}_{3-\delta}$ nanopowder. The addition of ammonium nitrate in the combustion precursor gel, as oxidizer agent and to trigger the combustion, was evaluated. A detailed morphological, structural and textural characterization of the nanostructured LSCM materials was performed. The next aim is the bottom-up building process of LSCM nanoelectrodes in symmetrical-SOFC. The attention is focused to keep as much as possible the nanostructured nature of the starting LSCM powders in the final morphology of the electrodes in the symmetrical (LSCM/LSGMg/LSCM) cells. Finally, preliminary electrocatalytic testing of the symmetrical cells in both oxidizing and reducing symmetric atmospheres for electrodes with different crystallite size are presented and discussed.

2. Experimental section

2.1. Synthesis of electrode material

Nanostructured powders of $\text{La}_{0.75}\text{Sr}_{0.25}\text{Cr}_{0.5}\text{Mn}_{0.5}\text{O}_{3-\delta}$ composition were prepared by combustion synthesis employing glycine as fuel and complexing agent, and ammonium nitrate as trigger to promote the combustion process. Glycine is known to act as a complexing agent for a number of metal ions, as it has a carboxylic acid group at one end and an amino group at the other end [31]. This zwitterionic characteristic of the glycine molecule enables the effective formation of complexes with metal ions of varying ionic sizes. These complexes help to maintain compositional homogeneity among the constituents by preventing their selective precipitation. On the other hand, glycine also serves as a fuel in the combustion reaction, as it is oxidized by nitrate ions. Glycine acts as a fuel during the combustion reaction, being oxidized by the nitrate ions. Oxygen from air does not play an important role during this combustion process [35]. On the other hand, ammonium nitrate is often chosen as a combustion aid in combustion synthesis because of its low cost and highly exothermic decomposition. Also, generates gaseous products only, without altering the proportion of other elements that are produced [32].

In a typical procedure, stoichiometric amounts of La_2O_3 (Alfa Aesar, 99.99%), SrCO_3 (Alfa Aesar, 99%), $\text{Cr}(\text{NO}_3)_3 \cdot 9\text{H}_2\text{O}$ (Alfa Aesar, 98.5%) and metallic Mn (Alfa Aesar, 99.99%) were dissolved in a HNO_3 (Cicarelli, 65%) diluted solution. In order to obtain the nitrates mixture, the metal ions solution was heated at $T \sim 80\text{ }^{\circ}\text{C}$ during 24 h. Then, distilled water, $\text{NH}_2\text{CH}_2\text{COOH}$ (Aldrich, 98%) and NH_4NO_3 (Mallinckrodt, 99.99%) were added to the dried metal-nitrates mixture. The glycine ($\text{NH}_2\text{CH}_2\text{COOH}$) content was adjusted to an elemental stoichiometric coefficient (ϕ) equal to 1.8, according to the results reported elsewhere [34]. The ϕ coefficient is defined as the ratio between the total valences of the fuel

(C₂H₅NO₂) and the total valences of the oxidizers (nitrates) [34]. The influence of NH₄NO₃ in the initial synthesis gel over the final structural properties was evaluated. The obtained solutions (with and without NH₄NO₃) were transferred to a glass ball, which was placed in a preheated “electric heating case” and kept at 250 °C. During the final stage of the evaporation, the solution began to swell forming a viscous foam, followed subsequently by the spontaneous combustion of the precursor with the release of a large amount of gases. The La_{0.75}Sr_{0.25}Cr_{0.5}Mn_{0.5}O_{3-δ} phase evolution was evaluated subjecting the as-synthesized nanopowders to thermal treatments during 6 h in air atmosphere in a furnace at 500, 700 and 1000 °C (heating rate of 5 °C min⁻¹). The powder samples were labeled LSCM(ss) without and with “-Aid”, i.e. absence/presence of ammonium nitrate in the precursor gel, respectively, and “ss” indicates the synthesis stage, from the as-synthesized materials (as) to the subsequent thermal treatment applied (500, 700 and 1000 °C during 6 h).

2.2. Cell construction

To test the electrode behavior, a symmetrical 2-electrode configuration, using LSGMg (La_{0.8}Sr_{0.2}Ga_{0.8}Mg_{0.2}O_{3-δ}, Next Tech Materials Ltd.) as electrolyte, was employed. Dense LSGMg disks of ~1 mm thickness and ~10 mm diameter were obtained after uniaxially pressing powder at 7.35 MPa, and then sintered at 1400 °C for 6 h. Inks for electrode deposition were prepared using 100 mg of LSCM (nano- or fine-powder), 13 mg of PVB (polyvinyl butyral, Aldrich) as binder, 10 mg of PVP (polyvinylpyrrolidone, Alfa Aesar) as dispersant and 59 mg of α-terpineol (95%, Alfa Aesar) as densifier, in an isopropylic alcohol medium. Three LSCM-ink layers were deposited onto both surfaces of the LSGMg electrolyte by the spin coating technique. The film depositions were performed at ambient conditions and each ink layer was dried at 165 °C. In order to obtain different electrode morphology of the symmetrical cells, experimental parameters such as LSCM crystallite size and “quick-stuck” thermal treatments of the inks-pellets have been modified: Cell-95 and Cell-165 were constructed by employing LSCM(500)-Aid nanocrystallites, being then placed and maintained during 10 and 30 min in a preheated furnace at 1000 °C, respectively; whereas for the Cell-365, LSCM(1000)-Aid fine-crystallites were employed in the ink and then it was thermally treated at 1000 °C during 30 min in the preheated furnace. The cells were labeled Cell-xxx, where “xxx” is the average crystallite size into the electrode material.

2.3. Characterization techniques

The nanostructured LSCM materials were characterized by X-ray diffraction (XRD), nitrogen adsorption/desorption, scanning electron microscopy (SEM), transmission electron microscopy (TEM) and electrochemical impedance spectroscopy (EIS).

XRD patterns were collected in air, at room temperature, on a Philips PW 1700 diffractometer by using Cu K(α1 + α2) lines and a graphite monochromator. Diffraction data were recorded in the range of 2θ between 10 and 99° at an interval of 0.02° and a dwell time of 13 s.

The lattice parameters and the average apparent crystallite size for each sample were determined from powder X-ray diffractograms by employing the Rietveld method and the FULLPROF program [36–38]. The XRD patterns were refined on the basis at trigonal/rhombohedral crystalline system in the R-3c space group (N° 167), in agreement with the ICSD Collection Code N° 157857 [39]. The initial structural parameters for Rietveld refinement were taken from the mentioned reference. The refined parameters were the scale factor, background, shift lattice constants, profile half-

width parameters (U, V, W, X and Y), isotropic thermal factors, occupancy and atomic functional positions. The background was adjusted using a linear interpolation between several points manually chosen. The diffraction peak profiles were fitted by the Thompson–Cox–Hastings pseudo-Voigt (pV-TCH) function and the asymmetry function described by Finger et al. [40].

Specific surface areas and pore size distributions were determined from N₂ adsorption/desorption isotherms obtained at 77 K using a Micromeritics ASAP 2020 (Accelerated Surface Area and Porosimetry System). The surface area was determined by the Brunauer, Emmett, and Teller (BET) method. The pore size distribution, obtained for the adsorption branch, was calculated by the Barrett, Joyner, and Halenda (BJH) method, based on the Kelvin equation.

The morphology of LSCM perovskites was determined by scanning electron microscopy (SEM) using a FEI Field-Emission Gun (FEG) in a Nova NANO-SEM 230 equipment, operating at 5 kV and an electron landing energy of 1 keV. These conditions were used in order to observe insulator materials without any conducting coating.

Microstructure and morphology at high magnifications were studied using Transmission Electron Microscopy (TEM) and High Resolution TEM (HR-TEM). Powder samples were dispersed in isopropanol and ultrasonicated for 15 min. After that two or three drops were deposited over ultrathin carbon support films TEM grids and let dry in air. The images were obtained using a Philips CM 200 UT microscope equipped with an ultra-twin objective lens. The electron source used was a LaB₆ filament operated at 200 keV. The nominal resolution was 2 Å for the HR-TEM mode. The microscope was equipped with a CCD camera for image digital acquisition. The contrast and illumination were adjusted linearly afterward using commercially available image treatment programs. Statistics on the crystallites was performed with the programs Image J 1.43U and Origin® 8.0. Crystallite size is given as the mathematical average ± standard deviation (±SD) of the largest crystallite dimension.

Area specific resistance (ASR) electrode values were determined from electrochemical impedance spectroscopy (EIS) under symmetric atmospheres (synthetic air or wet 20% H₂–Ar) using a frequency response potentiostat/impedance analyzer AUTOLAB PGSTAT-30. The ASR values obtained from symmetrical measurement under the same gas composition (without chemical potential gradient) can be different to those obtained from fuel cell tests [7]. This is due to the fact that SOFC operates under an oxygen chemical potential gradient with oxidant and reducing gases in the cathode and anode respectively, and the current across the cell affects the polarization of both electrodes. Nevertheless, the symmetrical cell electrode measurement is a useful and easy method to compare different materials. The impedance spectra were recorded over a frequency range 10⁶ to 0.01 Hz with signal amplitude of 10 mV under open circuit conditions. The electrochemical cells prepared with symmetrical configuration were placed and slightly pressed on porous electrodes between platinum grids, which were used as current collectors. In contrast to the almost all experimental settings reported in literature [7,12,17,41], no additional Pt or Au coatings onto electrode surfaces were applied, in order to avoid any additional catalytic effect. These coatings improve the electron transport limitations, possibly by introducing errors in the actual values of the electrode polarization resistance. The EIS measurements were carried out both of 0.2O₂–0.8Ar vol.% and 0.17H₂–0.03H₂O–0.8Ar vol.% atmospheres, heating and maintaining the cells at 800 °C until 30 h. The flow rate of gases was about 100 mL min⁻¹. The water content in the reducing flow was controlled by electrochemical cell (Pt/YSZ/Pt), which injected O₂ from atmospheric air to the 0.2H₂–0.8Ar flow [42].

3. Results and discussions

3.1. Synthesis of pure-phase LSCM nanocrystallites

Fig. 1 presents the XRD patterns of the LSCM nano-perovskites prepared in fuel-rich conditions from an elemental stoichiometric coefficient $\varphi = 1.8$ [34], showing the influence of NH_4NO_3 in the starting solution on the final structure of the materials. This figure presents the XRD patterns of the as-synthesized (as) nanopowders as well as the same thermally treated at 700 and 1000 °C. As it can be seen in Fig. 1(A), when the synthesis was performed without the adding of NH_4NO_3 in the initial synthesis gel, the LSCM perovskite-phase was obtained after the combustion but the presence of an additional organic amorphous phase can also be observed [43,44]. For these conditions, a non-flame smothering combustion took place and only occasional sparks can be observed. The auto-combustion was conducted in a gentle manner and lasted several seconds. The carbonaceous amorphous residues remained after combustion possibly due to the insufficient quantity of oxidizers species. Then, when a thermal treatment at 700 °C during 6 h was applied at these LSCM(as) nanopowders, several impurities were formed: SrCrO_4 (PDF N° 00-011-0519), MnCO_3 (PDF N° 00-007-0268), SrCO_3 (PDF N° 00-001-0556), Sr_2CrO_4 (PDF N° 00-019-1206) and La_2C_3 (PDF N° 01-082-0622). Only a thermal treatment at 1000 °C during 6 h causes the pure-phase $\text{La}_{0.75}\text{Sr}_{0.25}\text{Cr}_{0.5}\text{Mn}_{0.5}\text{O}_{3-\delta}$ formation, as has been reported elsewhere [34].

On the other hand, when the NH_4NO_3 (1 g per gram of catalyst) assisted the auto-combustion process, a volumetric combustion happened simultaneously throughout the whole swelled foam, generating a vigorous flame during 3 or 4 s. As can be seen in Fig. 1(B), pure-phase $\text{La}_{0.75}\text{Sr}_{0.25}\text{Cr}_{0.5}\text{Mn}_{0.5}\text{O}_{3-\delta}$ nanocrystallites were formed directly after the combustion (LSCM(as)-Aid). Additionally, when this nanopowder was subjected to subsequent thermal treatments at 700 and 1000 °C, the purity of the LSCM phase was preserved. It can be said that the presence of the ammonium nitrate in the starting batch will accelerate the reaction: as the decomposition of NH_4NO_3 takes place at less than 250 °C, probably this intensive exothermic reaction will provide sufficient energy to trigger the complete auto-combustion [32,45]. It is worth to mention that the diffraction peaks of the LSCM(as)-Aid catalyst became sharper in comparison with the LSCM(as) catalyst, which indicates a grow in the nanocrystallites size. Additionally, different NH_4NO_3 contents (1, 2, and 4 g per gram of catalyst) in the initial synthesis gel were also evaluated (results not

Table 1

Structural and textural parameters of the as-synthesized LSCM nanopowders prepared without and with NH_4NO_3 (Aid) in the initial synthesis gel and its respective thermal treatments at 700 and 1000 °C during 6 h.

Sample	$S_{\text{BET}}^{\text{a}}$ ($\text{m}^2 \text{g}^{-1}$)	D_p^{b} (nm)	$a = b^{\text{c}}$ (\AA)	c^{c} (\AA)	V^{d} (\AA^3)	D^{e} (g cm^{-3})
LSCM(700)	18.41	14.31	5.5019	13.3162	349.085	6.59
LSCM(1000)	2.84	284.52	5.5002	13.3235	349.056	6.43
LSCM(as)-Aid	10.26	30.45	5.5005	13.3597	350.052	6.43
LSCM(700)-Aid	8.38	38.47	5.4955	13.3420	348.948	6.50
LSCM(1000)-Aid	2.59	302.13	5.5044	13.3314	349.806	6.40

^a Specific surface area calculated by BET method. Parameters obtained from Rietveld refinement:

^b Average crystallite size.

^c Direct cell parameters.

^d Unit cell volume.

^e Density (volumic mass). Fitting confidence: $\chi^2 < 3$, $R_{\text{Bragg}} < 3$, $R_p < 8$ and $R_{\text{wp}} < 9$.

showed here). The increasing amount of NH_4NO_3 employed in the precursor gel extended the flame duration from 3–4 s to ~10 s, when 1 and 4 g of NH_4NO_3 were employed, respectively [32]. This behavior generated the growing of crystallites from ~30 to ~60 nm. In this sense, Ge and co-workers [46] said that the temperature during the combustion is strongly affected by the NH_4NO_3 amount added to the initial synthesis gel. Therefore, the growing of the nanocrystallites could be the result of the co-participation of these two phenomena.

In order to determine the lattice parameters and the average apparent crystal size of the LSCM nanopowders, the XRD patterns were analyzed with the FULLPROF program by employing Rietveld refinement technique. This method employs the intensity profile obtained from step-scanning measurements of the ceramic to refine the structure model of a material [37]. Some results of the Rietveld refinements of $\text{La}_{0.75}\text{Sr}_{0.25}\text{Cr}_{0.5}\text{Mn}_{0.5}\text{O}_{3-\delta}$ powders are presented in Table 1. In addition, a representative Rietveld refinement of the LSCM(as)-Aid sample is shown in Fig. 2. The fitting parameter values (R_p , R_{wp} , R_{Bragg} , and χ^2) shown in Table 1, indicate a good agreement between the refined and observed XRD patterns for the LSCM phase, which confirms that the $\text{La}_{0.75}\text{Sr}_{0.25}\text{Cr}_{0.5}\text{Mn}_{0.5}\text{O}_{3-\delta}$ nanocrystallites belongs to trigonal/rhombohedral crystalline system in R-3c space group (N° 167). In addition, the Rietveld refinement results obtained in this study are in good agreement with those reported in the literature for LSCM ceramics [39]. On the other hand, the apparent crystallite sizes, D_p , of LSCM(as) nanopowders, also calculated from Rietveld

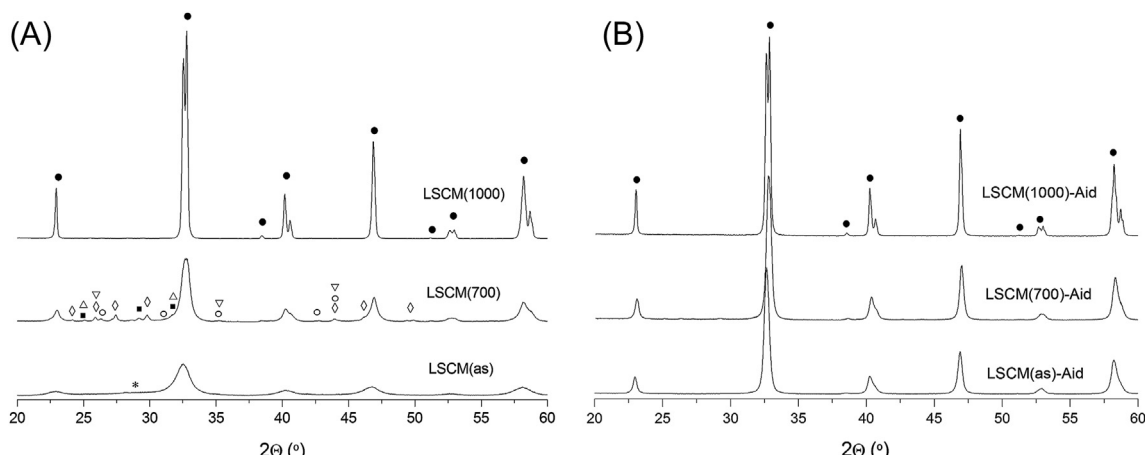


Fig. 1. XRD patterns of as-synthesized LSCM nanopowders prepared without (A) and with 1 g of NH_4NO_3 (B) per gram of catalyst, and its respective thermal treatments at 700 and 1000 °C. Phases present: ● $\text{La}_{0.75}\text{Sr}_{0.25}\text{Cr}_{0.5}\text{Mn}_{0.5}\text{O}_{3-\delta}$; ◇ SrCrO_4 ; ○ Sr_2CrO_4 ; △ MnCO_3 ; ▽ SrCO_3 ; ■ La_2C_3 .

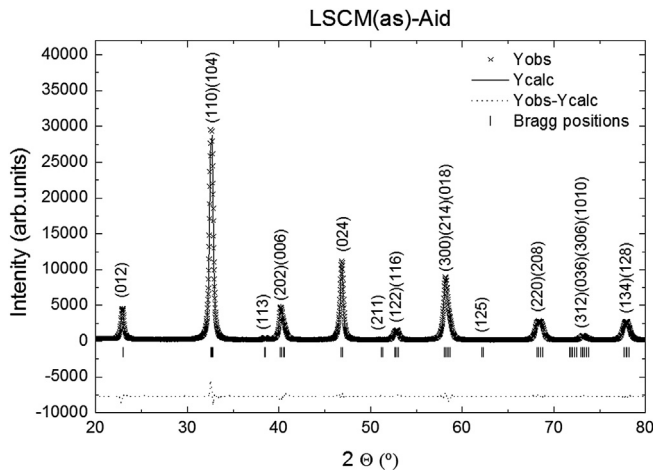


Fig. 2. Rietveld-refined XRD profile of LSCM(as)-Aid nanopowder. The \times signs represent experimental points and the solid line represents Rietveld-refined data. The dotted lines show the difference between experimental and refined data.

refinement, are shown in Table 1. As it can be observed, the average crystallite size of the as-synthesized LSCM nanopowders increases from ~ 6 to ~ 30 nm, when 1 g of NH_4NO_3 (per gram of final catalyst) was added to the starting batch. This behavior is probably due to the change of the combustion mode from non-flame smothering to flame-volumetric process. Then, when a heat treatment at 1000°C during 6 h was applied, the growth of the nanocrystallite size was similar for both LSCM(as) and LSCM(as)-Aid nanopowders.

Fig. 3 shows the N_2 physisorption isotherms of the as-synthesized $\text{La}_{0.75}\text{Sr}_{0.25}\text{Cr}_{0.5}\text{Mn}_{0.5}\text{O}_{3-\delta}$ nanopowders prepared without and with NH_4NO_3 (aid-combustion). Both materials exhibit type II isotherms in IUPAC classification, typical of macroporous

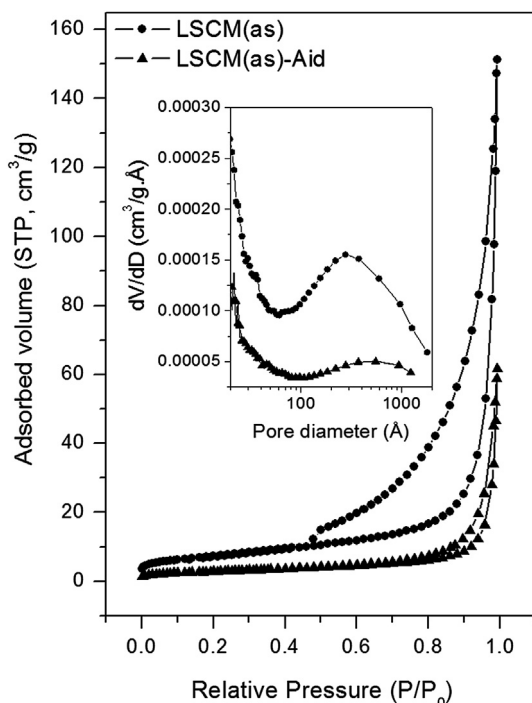


Fig. 3. Nitrogen physisorption isotherms and BJH pore size distribution (inset) of as-synthesized LSCM nanopowders prepared without (●) and with NH_4NO_3 (▲).

structures with stronger interactions with the adsorbate [47–49]. In addition, these isotherms exhibit a marked H3-type hysteresis loop in IUPAC classification, which do not exhibit any limiting adsorption at high p/p_0 [47]. This feature is characteristic of aggregates of plate-like crystallites giving rise to slit-shaped pores. In particular, the hysteresis loop of the LSCM(as) sample was extended to the intermediary pressure range, which indicates the presence of intercrystallite mesoporosity in addition to the macropore network. In fact, the inset of Fig. 3 shows a wide BJH-size distribution in the meso- and macroporous region for the LSCM(as) sample; while the LSCM(as)-Aid sample evidenced a marked decrease of the pore size distribution curve, which it is found predominantly in the macroporous region. The BET specific surface areas (S_{BET}) of as-synthesized LSCM samples are shown in Table 1. The pure-phase LSCM(as)-Aid material, synthesized employing NH_4NO_3 as combustion trigger agent and oxidizer, showed a lower specific surface area around $\sim 10 \text{ m}^2 \text{ g}^{-1}$ in comparison with the $\sim 26 \text{ m}^2 \text{ g}^{-1}$ presented by the LSCM(as) material prepared without ammonium nitrate in the initial synthesis gel. This behavior is due to the increase in the crystallite size from 6 to 30 nm, and probably also to the complete elimination of the organic amorphous phase.

Fig. 4 shows SEM images of as-synthesized LSCM nanopowders prepared without (a, b) and with NH_4NO_3 (c, d) in the initial synthesis gel. The LSCM(as) nanopowders, synthesized without ammonium nitrate, displayed sponge-like morphology, which would consist of small nanocrystallites aggregated with typical meso and macropores. The SEM images cannot resolve the crystallites since their sizes are too small (around 6 nm) and/or the grains boundaries do not present morphological contrast to be observed within the resolution of this technique. On the other hand, the LSCM(as)-Aid sample evidenced the presence of strongly interconnected nanocrystallites, with a relatively homogenous crystallite size, forming a porous structure with cavities mainly in the macroscale, which is in concordance with the XRD and N_2 physisorption results presented above.

The morphology and crystallinity of these as-synthesized LSCM nanopowders was further analyzed by TEM and HR-TEM images. As shown in the images (a–c) of Fig. 5, the LSCM(as) sample shows the presence of strongly aggregated nanocrystallites forming a foam structure with several cavities (low contrast randomly regions) in the mesoscale. Even considering that the LSCM(as)-Aid sample evidenced a bigger crystallite size and a lower porous structure in comparison with the sample prepared without ammonium nitrate, the images (d, e) show a mesoporosity between crystallites, which probably would help to the diffusion of the reactive gases into nanopowder. It is noteworthy that all these nanopowders are constituted by well-crystallized nanograin, where each grain is a single nanocrystal, i.e. within each crystallite, lattice images (individual atomic planes) show a single orientation. The images (b, c, e, f), of high magnification, also show some interface fringes, which are generated by the overlapping of nanocrystallites with lattice planes at different orientations.

In addition, crystallite-size distributions were calculated from the statistics taken from hundreds of crystalline domains of each sample using both high resolution and dark field images. As observed in the bottom of Fig. 5, the LSCM(as)-Aid sample evidenced a wide distribution crystallite size around 30 nm, whereas the LSCM(as) material shows a narrow distribution around of 6 nm; both results are very close to the values obtained by the Rietveld refinement.

3.2. Cell construction

XRD patterns of the precursor elements for the construction of the LSCM/LSGMg/LSCM cells, i.e. electrode precursor powders and

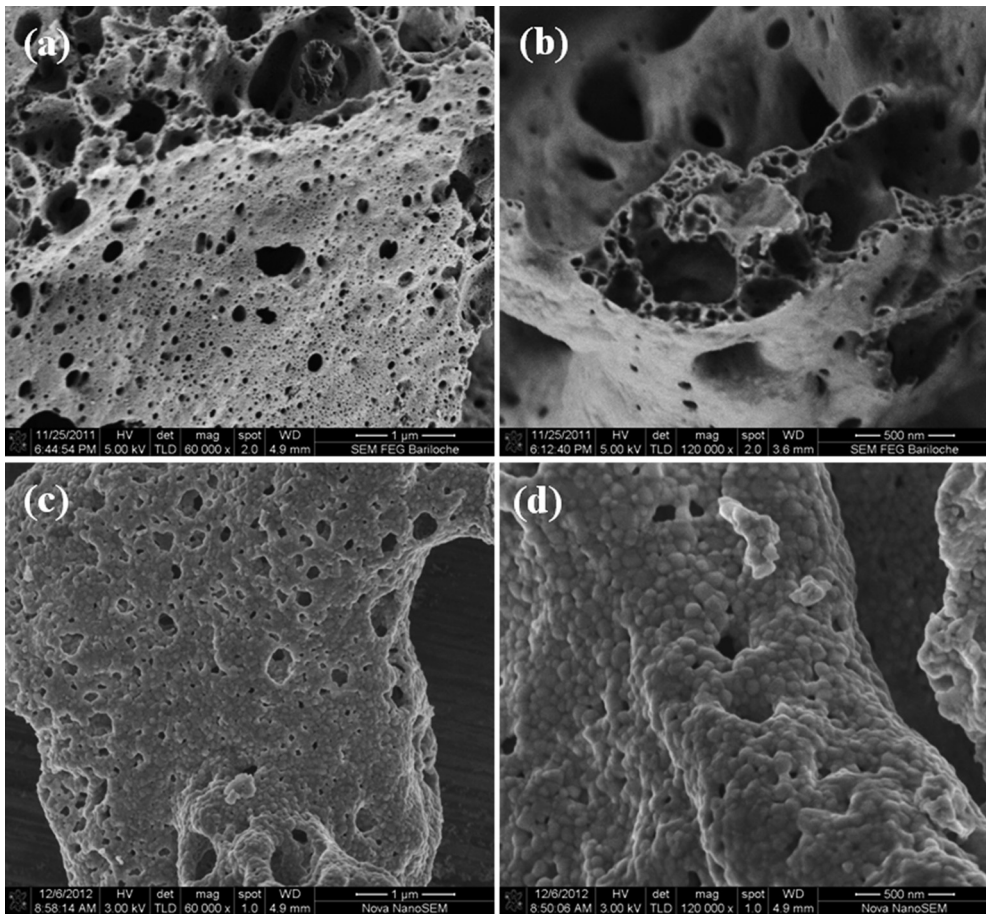


Fig. 4. SEM images of as-synthesized LSCM nanopowders prepared without (a, b) and with NH_4NO_3 (c, d) in the initial synthesis gel, shown at different magnitude order.

electrolyte disk sintered are shown in Fig. 6(A). As it was detailed in the experimental section, two precursor powders (nano and fine-crystallites) were employed to build different electrode morphologies. It is noteworthy that the LSCM(as)-Aid nanopowder was subjected to the thermal treatment in static air atmosphere at 500 °C during 6 h, in order to eliminate the possible carbonaceous residues from the chemical synthesis route. This thermal treatment did not modify the crystallite size neither its specific surface area in respect to LSCM(as)-Aid nanopowder. On the other hand, in order to obtain bigger crystallite size (fine-crystallites) to compare electrochemical activities, the LSCM(as)-Aid nanopowder was also subjected to thermal treatment in air static atmosphere at 1000 °C during 6 h. In addition, Fig. 6(B) presents the XRD pattern of the final electrode surface of the cells constructed. It can be observed that all electrode surfaces of the cells show only the peaks corresponding to the perovskite-type $\text{La}_{0.75}\text{Sr}_{0.25}\text{Cr}_{0.5}\text{Mn}_{0.5}\text{O}_{3-\delta}$ oxide phase. Therefore, it is demonstrated that by optimizing the synthesis conditions of the nanopowders and by employing quick-stuck thermal treatments for the inks, it is possible to build pure-phase $\text{La}_{0.75}\text{Sr}_{0.25}\text{Cr}_{0.5}\text{Mn}_{0.5}\text{O}_{3-\delta}$ nanoelectrodes.

Fig. 7 shows cross-section images of the representative electrode/electrolyte interfaces of the LSCM/LSGMg/LSCM symmetrical cells after the electrocatalytic testing. The electrodes show porous microstructures with adequate adherence to the LSGMg electrolyte disk. Although an equal mass of crystallites (1 g) was employed in all of LSCM-inks, the electrode thicknesses obtained in the final cells varied markedly. The electrode thickness of the Cell-365 (image-c), constructed from fine-crystallites, was

around $\sim 20 \mu\text{m}$, while for the Cell-95 (image-a) and Cell-160, constructed from nanocrystallites, were above to $40 \mu\text{m}$. This behavior indicates that the final porosity degree obtained in the electrodes constructed from nanocrystallites is bigger, which probably would enhance the diffusion of the reactive gases into the electrodes. It is noteworthy that no significant changes were observed in the electrode morphologies as in the electrode/electrolyte interfaces, after the cells were subjected to the electrocatalytic tests under both oxidizing and reducing atmospheres.

Fig. 8 shows images of internal morphology of the LSCM electrodes in the symmetrical cells after of the electrocatalytic testing; their average crystallite sizes and an approximation of their specific surface areas (S_{BET}) are presented in Table 2. The S_{BET} were measured in LSCM powders (nano and fine) subjected at the same thermal treatments employed to bond the inks over the electrolyte. By varying the experimental parameters, such as LSCM crystallite size and bonding thermal treatments of the inks-electrolyte, different electrode morphologies were obtained. All the electrodes are made of uniform crystallite with homogenous size distribution in the ranges between 95 and 325 nm. The electrode of the Cell-95 is constituted by well-interconnected nanocrystallites, while in the Cell-160 is formed by fine-crystallites partially sintered. The Cell-325 was built for comparative purpose in order to obtain electrode with markedly larger crystallites size. It is noteworthy that no appreciable change in the particle size distribution of the electrodes, before and after of the electrocatalytic testing, was evidenced. By using nanocrystallites in the ink-precursor, it can

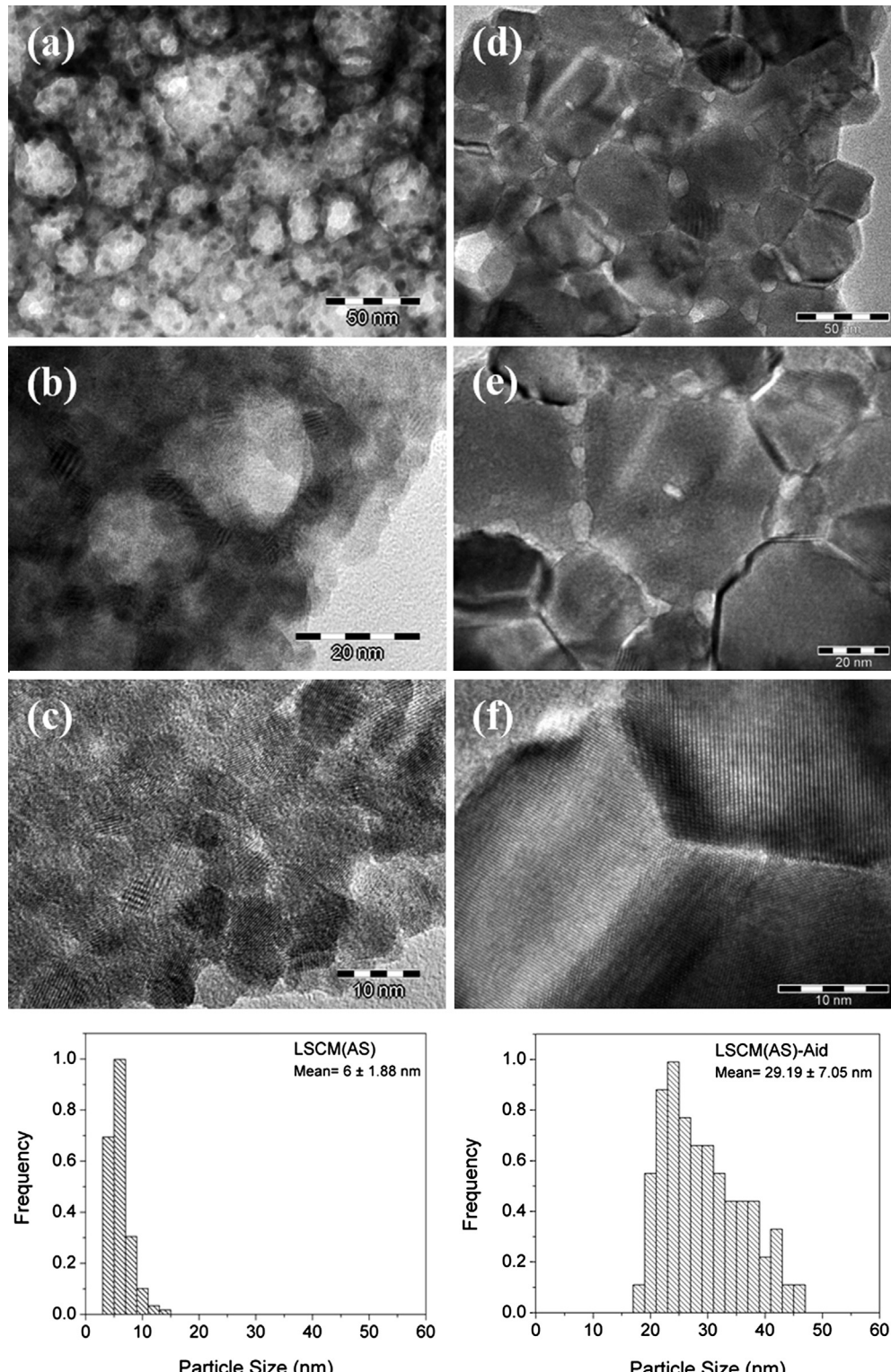


Fig. 5. TEM and HR-TEM images of as-synthesized LSCM nanpowders: (a–c) correspond to the sample prepared without "Aid", while (d–f) correspond to the sample prepared with 1 g of NH₄NO₃ per gram of catalyst. (a, d) Are low magnification images which depicts the porosity and the grain sizes. (b, c, e, f) Are images of greater magnification (HR-TEM), where the interphases between the grains are resolved. Its respective crystallite-size distributions are also shown at the bottom.

be constructed electrodes with crystallite size in the nanoscale, low densification, open porosity, adequate adherence with the electrolyte, and probably with sufficient integrity to enhance their electrocatalytic performance.

3.3. Electrocatalytic testing

The electrocatalytic behavior of the LSCM electrodes with different morphologies was evaluated by electrochemical

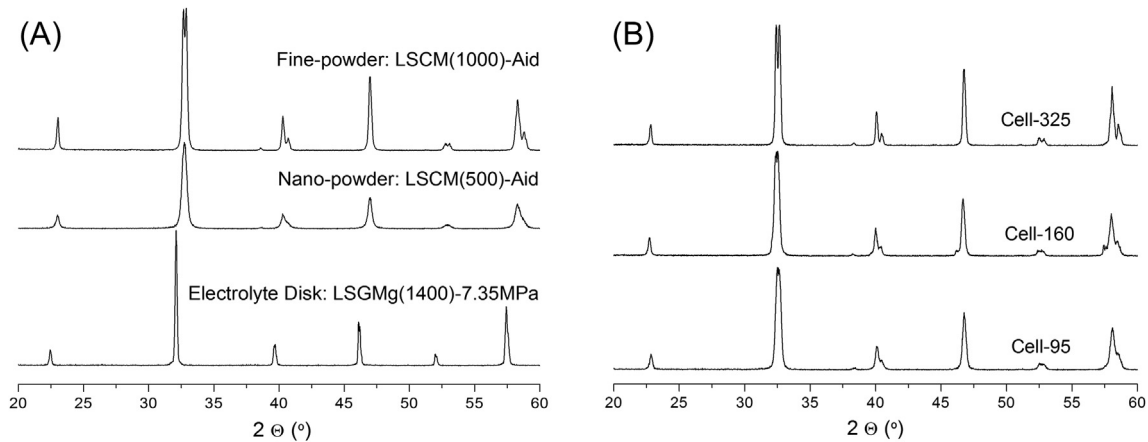


Fig. 6. XRD patterns of the precursor elements for the cells construction (A), and electrode surfaces of the symmetrical (LSCM/LSGMg/LSCM) cells with different electrode crystallite size (95, 160 and 325 nm) (B).

impedance spectroscopy (EIS) in symmetric (LSCM/LSGMg/LSCM) cells at 800 °C under symmetric atmospheres and zero dc polarization. The EIS spectra of the LSCM electrodes with different average crystallite sizes (95, 160 and 325 nm) obtained after 20 h, are presented in Fig. 9. For the sake of comparison, the series resistance determined from the high frequency intercept of the electrode impedance on the real axis in the Nyquist plane, which

represents the sum of the electrolyte resistance and additional contacts, has been subtracted. In order to obtain all of the electrode polarization resistance values, the impedance spectra were fitted with equivalent circuits employing the ZView 3.0 program [50]. The area specific resistance (ASR) of the electrodes was determined according to the following formulae for a symmetric cell: $ASR = R_p * A/2$ [51], where R_p is the electrode polarization

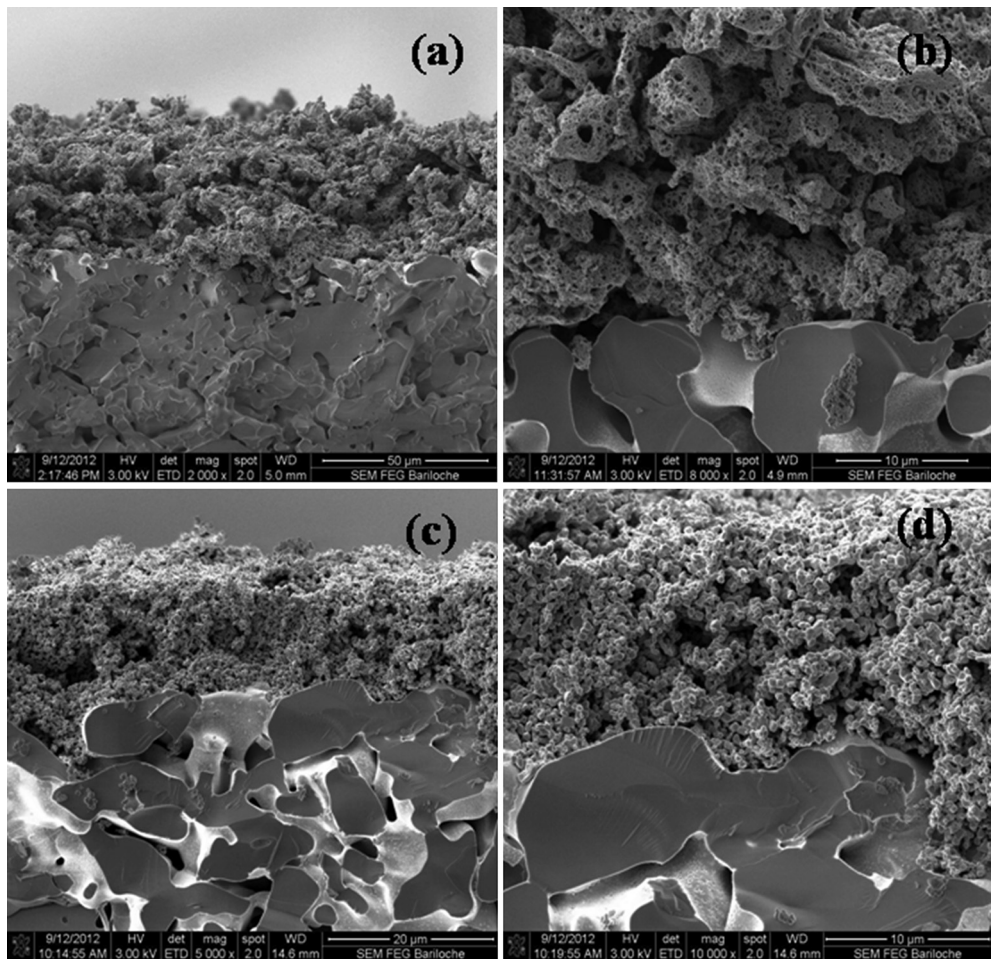


Fig. 7. SEM images of fractured cross-sections of the Cell-95 (a, b) and Cell-325 (c, d), after electrocatalytic testing, showed at different magnification.

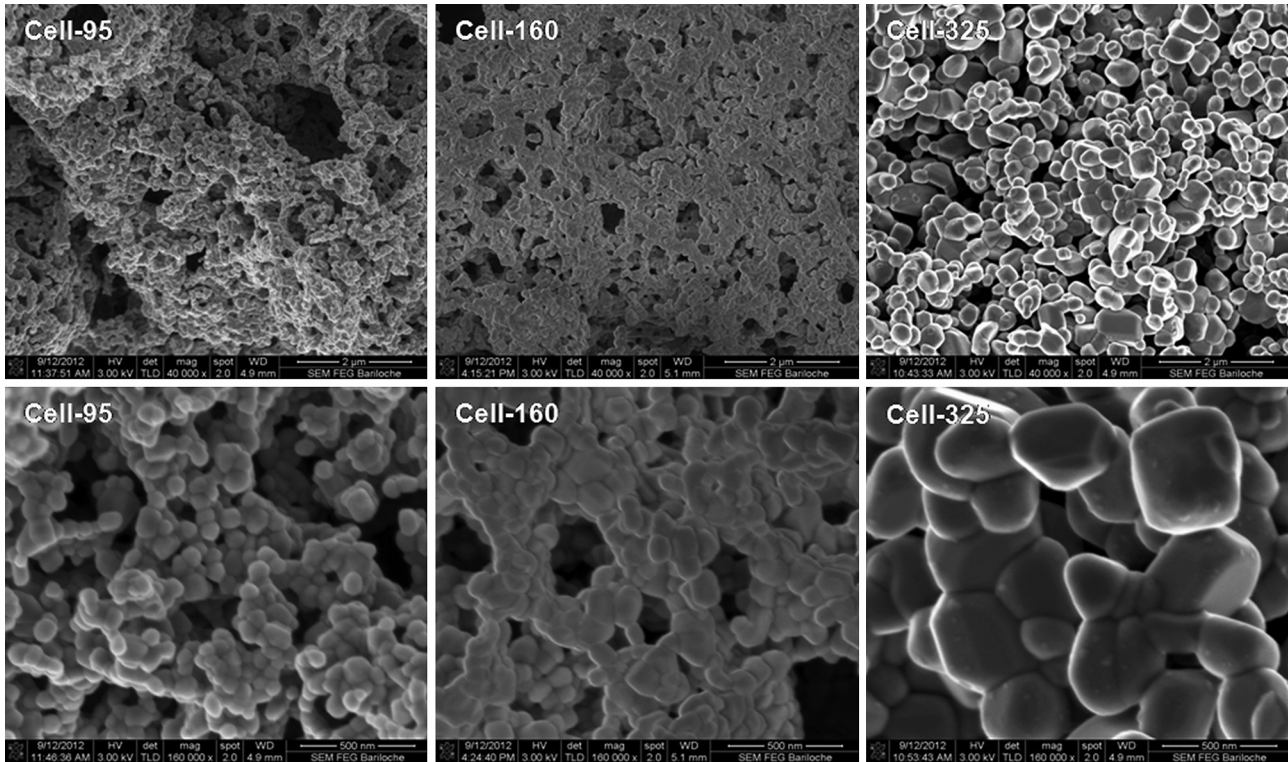


Fig. 8. SEM images of the different morphologies of LSCM electrodes obtained in the (LSCM/LSGMg/LSCM) cells, showed at different magnification.

Table 2

Electrode polarization resistances of symmetrical (LSCM/LSGMg/LSCM) cells with different electrode crystallite size (95, 160 and 325 nm), obtained after 20 h at 800 °C under symmetric oxidizing and reducing atmospheres.

Cells	D_p^a (nm)	$\sim S_{BET}^b$ ($\text{m}^2 \text{ g}^{-1}$)	ASR ($\Omega \text{ cm}^2$)	
			O ₂ –Ar	H ₂ –H ₂ O–Ar
Cell-95	95 ± 17	5.29	1.31	13.78
Cell-160	160 ± 29	3.95	2.32	9.28
Cell-325	325 ± 82	2.09	3.60	7.04

^a Calculated from SEM images employing histograms of particle size distributions.

^b Specific surface area calculated by BET method from N₂ physisorption measures of LSCM powder thermally treated.

resistance and A is the geometrical electrode area; R_p values were halved due to the symmetric configuration. The ASR values for the LSCM electrodes, by varying their morphologies, both oxidizing and reducing symmetric atmospheres, are presented in Table 2. As it can be seen, the lowest ASR values obtained, after 20 h at 800 °C, were 1.51 $\Omega \text{ cm}^2$ in oxidizing atmosphere for the Cell-95 and 7.04 $\Omega \text{ cm}^2$ in reducing atmosphere for Cell-325. Both ASR values are significantly lower than those reported in literature [41,52–55]. In particular, Kharton et al. [41] reported ASR values, for the (La_{0.75}Sr_{0.25})_{0.95}Cr_{0.5}Mn_{0.5}O₃ electrode employing (La_{0.9}Sr_{0.1})_{0.98}Ga_{0.8}Mg_{0.2}O₃– δ as electrolyte, of 24.1 and 35.6 $\Omega \text{ cm}^2$ at 800 °C in air and wet 0.1H₂–0.9N₂ atmospheres, respectively. These authors synthesized the LSCM electrode by the glycine-nitrate process, however, to obtain the pure phase they calcined the as-synthesized

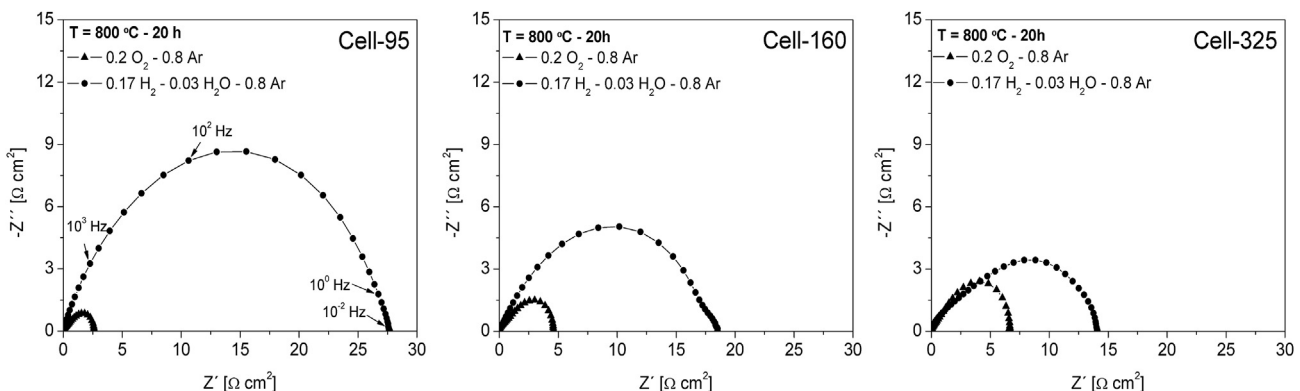


Fig. 9. Electrochemical impedance spectra of LSCM electrodes with different average crystallite size (95, 160 and 325 nm) collected after 20 h at 800 °C, in the symmetrical cells under symmetric atmosphere: oxidizing (▲) and reducing (●).

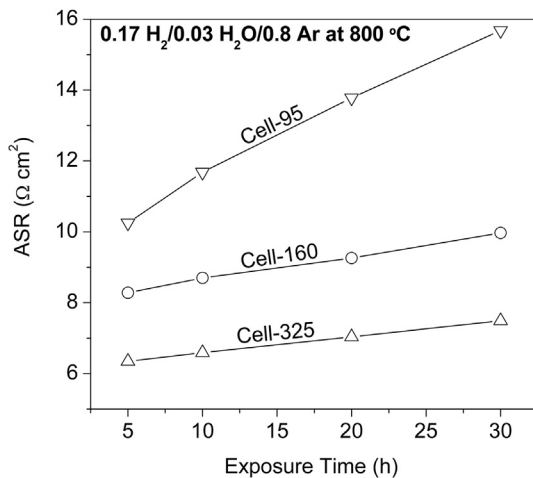


Fig. 10. Evolution of ASR values vs. exposure time under reducing atmosphere at 800 °C , for the cells with different electrode crystallite size (95, 160 and 325 nm).

material above 1300 °C . In the present study, since Pt grids were employed as current collectors, without any extra Au or Pt paste, the improvement on the polarization resistance values is mainly related to the microstructural optimization of the electrodes. As it can be seen in Table 2, in oxidizing atmosphere, the ASR values decrease when the crystallite size of the electrodes becomes smaller, whereas in reducing atmosphere it shows the opposite behavior, the ASR values increase when the crystallite size in the electrodes decreases. In addition, the cells exhibit lower total polarization resistance in oxidizing atmosphere than that obtained under reducing atmosphere, probably due to the fact that the limiting effect of charged carriers transport becomes even more pronounced for the reducing condition [41]. The electrocatalytic behavior as cathode, i.e. in oxidizing atmosphere, is probably due to the enlarging of the exposure surface generated by the crystallite-size decrease, with the consequent increase of the triple-phase boundary (TPB) in the electrode/electrolyte interface. On the other side, the electrocatalytic testing as anode, i.e. in reducing atmosphere, evidence possibly a degradation degree of the LSCM phase: the reduction of crystallite size also increases such undesired reactivity of the electrode material, but this time, negatively influencing the electrocatalytic response.

In order to investigate the stability of the LSCM material in $0.2\text{O}_2-0.8\text{Ar}$ and $0.17\text{H}_2-0.03\text{H}_2\text{O}-0.8\text{Ar}$ atmospheres at 800 °C , EIS spectra were collected as a function of exposure time (between 5 and 30 h). In oxidizing conditions, the ASR values were remained practically constant for the three cells, in all the time range of our test. Nevertheless, this behavior was not the same under reducing conditions. Fig. 10 presents the evolution of the ASR values vs. the exposure time in reducing atmosphere for the symmetrical cells. As it can be seen, all the symmetrical cells evidenced an increase in the ASR values with the exposure time under reducing conditions. However, the Cell-95 showed a marked increase, around 50%, in the ASR values respect to those of Cell-160 and Cell-325, which only showed an increase nearly 20% in its electrode polarization resistance. These behaviors are probably due to the lower thermodynamic stability (or bigger undesired reactivity) of nanocrystallites ($<100 \text{ nm}$) respect to fine-crystallites ($>100 \text{ nm}$) under reducing conditions.

Fig. 11(A) presents the XRD pattern of the electrode surfaces of the symmetrical cells after anodic testing (AT), i.e. 30 h in $0.17\text{H}_2-0.03\text{H}_2\text{O}-0.8\text{Ar}$ atmosphere at 800 °C . As it can be observed, only the XRD patterns of the Cell-95 and Cell-160 show an extra-peak compatible to $\text{A}_2\text{BO}_4\text{O}_\delta$ Ruddlesden–Popper (RP) phase, which could to correspond to $\text{Sr}_2\text{MnO}_{3.84}$ (PDF N° 01-081-1880), $\text{La}_2\text{MnO}_{4.15}$ (PDF N° 00-040-0002), La_2MnO_4 (PDF N° 00-033-0897), Sr_2MnO_4 (PDF N° 00-024-1222) and/or Sr_2CrO_4 (PDF N° 00-027-1436) phases. It is noteworthy that the peaks-intensity of the RP phase increases when the electrode particle size becomes smaller, which probably would evidence the undesired reactivity of the LSCM phase under reducing conditions, mentioned above. An RP phase is formed from a perovskite-like oxide by the inclusion of additional AO layers between the perovskite lattice layers, where $\text{A} = \text{La}$ or Sr in this case, making a layered perovskite structure [56]. RP phases are thermodynamically more stable than perovskite ones in reducing environment due to a lower valence state of manganese than in parent perovskite structure [57]. In agreement with these results, some authors reported that especially the La-rich part of the LSM family, generally decomposes under reducing conditions at high temperature into $(\text{La},\text{Sr})_2\text{MnO}_4$ and MnO [52,58], although a more complete dissociation with formation of La_2O_3 and an SrMnO_3 -type phase has also been observed [59,60]. In addition, Fonseca et al. reported for LSCM, a partial decomposition into $(\text{La},\text{Sr})_2(\text{Cr},\text{Mn})\text{O}_4$ after firing in pure H_2 for 5 h at 1000 °C , while a treatment at 800 °C , for the same period time, resulted in no detectable degradation of the LSCM phase [61]. It is noteworthy

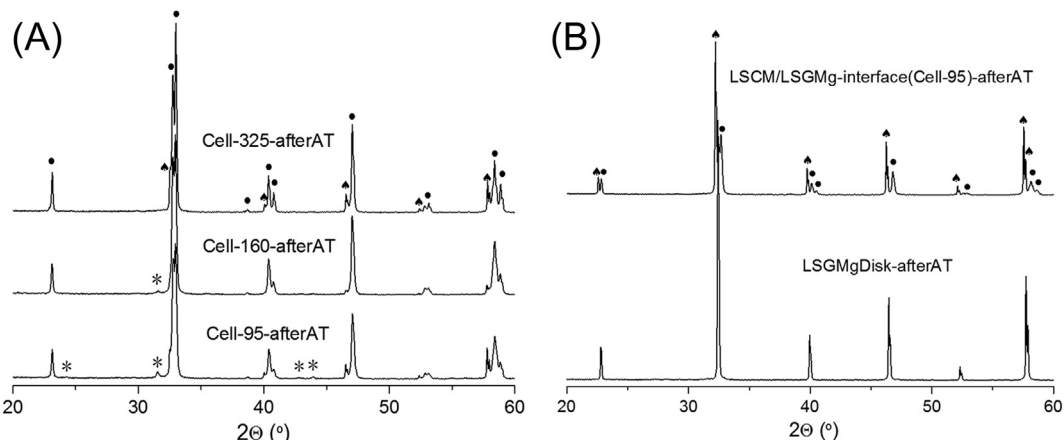


Fig. 11. XRD patterns of the cells components after anodic testing (AT), i.e. after 30 h at 800 °C in $0.17\text{H}_2-0.03\text{H}_2\text{O}-0.8\text{Ar}$ atmosphere. (A) Electrode surface of cells with different crystallite size (95, 160 and 325 nm); and (B) electrode/electrolyte interface of the Cell-95 and electrolyte disk. Phases present: ● LSCM; ▲ LSGM; * $(\text{La},\text{Sr})_2(\text{Cr},\text{Mn})\text{O}_4\pm\delta$.

that these authors obtained the pure LSCM phase after sintering at 1400 °C and consequently the crystallite sizes are within the range of micrometers. van den Bossche and McIntosh also reported, by XRD measurements, the formation of the RP phase when the LSCM material was thermally treated under reducing conditions (CH_4/N_2 and H_2/N_2) at 800 °C, being increased its intensity to high temperature treatments [62]. Therefore, all of these results suggest that the LSCM phase degradation would be strongly related with the particle size being increased for small particles and therefore observable even at 800 °C. Additionally, it is worth to mention that XRD measurements were also performed for the symmetrical cells after cathodic testing (not showed here), which only evidenced the characteristic peaks of the LSCM phase.

Finally, in order to infer the electrolyte reactivity in reducing conditions, a sintered LSGM disk was subjected to the same reducing conditions that the symmetrical cells, and to infer the electrode/electrolyte reactivity, some electrode layers of the Cell-95, previously subjected to anodic testing, were removed of the electrolyte surface. Fig. 11(B) shows XRD patterns of the electrode/electrolyte interface of the Cell-95 and disk LSGM electrolyte after 30 h under $0.17\text{H}_2-0.03\text{H}_2\text{O}-0.8\text{Ar}$ atmosphere at 800 °C. As it can be seen, none extra-peaks are observed in the XRD patterns, neither for the electrode/electrolyte interface nor for the electrolyte disk, which demonstrate that the LSCM does not react with the LSGM electrolyte under typical SOFC operating conditions.

4. Conclusions

In the present study, LSCM nanopowders have been successfully synthesized by the low-temperature auto-combustion method by using glycine as fuel and complexing agent, and ammonium nitrate as oxidizer and combustion trigger. By employing a stoichiometric elemental coefficient (φ) equal to 1.8, and 1 g of ammonium nitrate in the combustion precursor gel, pure-phase $\text{La}_{0.75}\text{Sr}_{0.25}\text{Cr}_{0.5}\text{Mn}_{0.5}\text{O}_{3-\delta}$ nanocrystallites were obtained. These as-synthesized pure-phase LSCM nanopowders consist of strongly aggregated nanocrystallites forming a sponge-like structure. The average nanocrystallite size of the pure-phase LSCM was around 30 nm, and its specific surface area was around $10\text{ m}^2\text{ g}^{-1}$. Crystalline structural analyses showed that the LSCM nanopowders present a trigonal/rhombohedral symmetry in the $R-3c$ space group. Electrodes with crystallite size in the nanoscale were built by employing these LSCM nanocrystallites in the precursor ink and quick-stuck thermal treatments of the inks-electrolyte. This nanoelectrodes presented low densification, open porosity, good connectivity between particles, adequate adherence with the electrolyte, and uniform grain with homogenous size distribution. These properties are desired in order to maximize the length of the triple-phase boundaries of the cathode and/or anode, which would be useful to decrease the electrode polarization resistance during SOFC operation. The ASR values obtained were $1.31\text{ }\Omega\text{ cm}^2$ in oxidizing atmosphere for the Cell-95, and $7.04\text{ }\Omega\text{ cm}^2$ in reducing atmosphere for the Cell-325, both at 800 °C after 20 h of exposition, which are significantly lower than those reported in literature, but it is worth to mention that are still too high for practical applications. In oxidizing atmosphere, the ASR values decrease when the crystallite size of the electrodes becomes smaller, while in reducing atmosphere, these values increase when the crystallite size of the electrodes decreases. The first behavior was related with the increase of the TPB in the electrode/electrolyte interface under oxidation condition, and the latter behavior was associated to the thermodynamic instability of the LSCM phase under anodic condition, in agreement with traces of Ruddlesden–Popper $\text{A}_2\text{BO}_{4\pm\delta}$ phase observed after EIS measurements.

Acknowledgments

This work was supported by CNEA and CONICET of Argentina. C. M. Ch. thanks to Dr. Jesus Vega-Castillo (CONICET fellowship) and Dr. Fabricio Ruiz (CONICET Researcher) by their valuable help on electrocatalytic activities, to Dr. Fabiana Gennari by the N_2 physisorption measurements and to Mr. Carlos Cotaro by the SEM images.

References

- [1] N.Q. Minh, T. Takahashi, *Science and Technology of Ceramic Fuel Cells*, Elsevier, Amsterdam, 1995.
- [2] S.C. Singhal, K. Kendall, *High Temperature Solid Oxide Fuel Cells*, Elsevier, Oxford, 2004.
- [3] J.B. Goodenough, Y.H. Huang, *J. Power Sources* 173 (2007) 1–10.
- [4] A. Atkinson, S.A. Barnett, R.J. Gorte, J.T.S. Irvine, A.J. McEvoy, M. Mogensen, S.C. Singhal, J.M. Vohs, *Nat. Mater.* 3 (2004) 17–27.
- [5] C.W. Sun, U. Stimming, *J. Power Sources* 171 (2007) 247–260.
- [6] J.C. Ruiz-Morales, J. Canales-Vázquez, D. Marrero-López, D. Pérez-Coll, J. Peña-Martínez, P. Núñez, *J. Power Sources* 177 (1) (2008) 154–160.
- [7] J.C. Ruiz-Morales, J. Canales-Vázquez, J. Pena-Martínez, D. Marrero-López, P. Núñez, *Electrochim. Acta* 52 (2006) 278–284.
- [8] A. El-Himri, D. Marrero-López, J. Carlos Ruiz-Morales, J. Peña-Martínez, P. Núñez, *J. Power Sources* 188 (2009) 230–237.
- [9] J.C. Ruiz-Morales, H. Lincke, D. Marrero-López, J. Canales-Vázquez, P. Núñez, *Bol. Soc. Esp. Ceram. Vidr.* 46 (4) (2007) 218–223.
- [10] J.C. Ruiz-Morales, J. Canales-Vázquez, B. Ballesteros, J. Peña-Martínez, D. Marrero-López, J.T.S. Irvine, *J. Eur. Ceram. Soc.* 27 (2007) 4223–4227.
- [11] J. Canales-Vázquez, J.C. Ruiz-Morales, D. Marrero-López, J. Peña-Martínez, P. Núñez, P. Gómez-Romero, *J. Power Sources* 171 (2007) 552–557.
- [12] S. Tao, J.T.S. Irvine, *J. Electrochem. Soc.* 151 (2004) A252–A259.
- [13] J. Liu, B. Madsen, Z. Ji, S. Barnett, *Electrochim. Solid State Lett.* 5 (2002) A122–A124.
- [14] S. Zha, P. Tsang, Z. Cheng, M. Liu, *J. Solid State Chem.* 178 (2005) 1844–1850.
- [15] S. Tao, J.T.S. Irvine, J.A. Kilner, *Adv. Mater.* 17 (2005) 1734–1737.
- [16] D.M. Bastidas, S. Tao, J.T.S. Irvine, *J. Mater. Chem.* 16 (2006) 1603–1605.
- [17] J. Peña-Martínez, D. Marrero-López, J.C. Ruiz-Morales, C. Savaniu, P. Núñez, J.T.S. Irvine, *Chem. Mater.* 18 (2006) 1001–1006.
- [18] S.P. Jiang, X.J. Chen, S.H. Chan, J.T. Kwok, K.A. Khor, *Solid State Ionics* 177 (2006) 149–157.
- [19] K. Sasaki, J.P. Wurtz, R. Gschwend, M. Gödickemeier, L.J. Gauckler, *J. Electrochem. Soc.* 143 (1996) 530–543.
- [20] S.P. Jiang, L. Zhang, Y.J. Zhang, *J. Mater. Chem.* 17 (2007) 2627–2635.
- [21] S.W. Tao, J.T.S. Irvine, *Nat. Mater.* 2 (2003) 320–323.
- [22] N.Q. Minh, J. Am. Ceram. Soc. 76 (1993) 563–588.
- [23] S. Carter, A. Selcuk, R.J. Chater, J. Kajda, J.A. Kilner, B.C.H. Steele, *Solid State Ionics* 59 (1992) 53–56.
- [24] V.V. Kharton, F.M.B. Marques, A. Atkinson, *Solid State Ionics* 174 (2004) 135–149.
- [25] S. Tao, J.T.S. Irvine, *Chem. Mater.* 18 (2006) 5453–5460.
- [26] E.S. Raj, J.A. Kilner, J.T.S. Irvine, *Solid State Ionics* 177 (2006) 1747–1752.
- [27] S.M. Plint, P.A. Connor, S. Tao, J.T.S. Irvine, *Solid State Ionics* 177 (2006) 2005–2008.
- [28] A. Ghosh, A.K. Azad, J.T.S. Irvine, *ECS Trans.* 35 (2011) 1337–1343.
- [29] T. Delahaye, T. Jardiel, O. Joubert, R. Lacournet, G. Gauthier, M.T. Caldes, *Solid State Ionics* 184 (2011) 39–41.
- [30] J.C. Ruiz-morales, J. Canales-Vázquez, H. Lincke, J. Peña-Martínez, D. Marrero-López, D. Pérez-Coll, J.T.S. Irvine, P. Núñez, *Bol. Cerám. Soc. Esp. Ceram. Vidr.* 47 (2008) 183–188.
- [31] L.A. Chick, L.R. Pederson, G.D. Maupin, J.L. Bates, L.E. Thomas, G.J. Exarhos, *Mater. Lett.* 10 (1990) 6–12.
- [32] A. Civera, M. Pavese, G. Saracco, V. Specchia, *Catal. Today* 83 (2003) 199–211.
- [33] J.L. Bates, L.A. Chick, W.J. Weber, *Solid State Ionics* 52 (1992) 235–242.
- [34] C.M. Chanquía, J.E. Vega-Castillo, A.L. Soldati, H. Troiani, A. Caneiro, *J. Nanopart. Res.* 14 (2012) 1104.
- [35] Z. Shao, W. Zhou, Z. Zhu, *Prog. Mater. Sci.* 57 (2012) 804–874.
- [36] R.A. Young, *The Rietveld Method*, International Union of Crystallography & Oxford University Press, New York, 1996.
- [37] H.M. Rietveld, *J. Appl. Crystallogr.* 2 (1969) 65–71.
- [38] J. Rodríguez-Carvajal, *Phys. B Cond. Matter* 192 (1993) 55–69.
- [39] S. Esterimirova, A. Fetisov, V. Balakirev, S.J. Titova, *Supercond. Nov. Magn.* 20 (2007) 113–116.
- [40] L.W. Finger, D.E. Cox, A.P. Jephcoat, *J. Appl. Crystallogr.* 27 (1994) 892–900.
- [41] V.V. Kharton, E.V. Tsipis, I.P. Marozau, A.P. Viskup, J.R. Frade, J.T.S. Irvine, *Solid State Ionics* 178 (2007) 101–113.
- [42] A. Caneiro, M. Bonnat, J. Fouletier, *J. Appl. Electrochem.* 11 (1981) 83–90.
- [43] H. Najjar, H. Batis, *Appl. Catal. A* 383 (2010) 192–201.
- [44] H. Najjar, J.F. Lamontier, O. Mentré, J.M. Giraudon, H. Batis, *Appl. Catal. B* 106 (2011) 149–159.
- [45] L. Ge, R. Ran, Z. Shao, Z.H. Zhu, S. Liu, *Ceram. Int.* 35 (2009) 2809–2815.

[46] L. Ge, W. Zhou, R. Ran, Z. Shao, S. Liu, *J. Alloys Compd.* 450 (2008) 338–347.

[47] K.S.W. Sing, D.H. Everett, R.A.W. Haul, L. Moscou, R.A. Pierotti, J. Rouquerol, T. Siemieniewska, *Pure Appl. Chem.* 57 (1985) 603–619.

[48] K. Traina, M.C. Steil, J.P. Pirard, C. Henrist, A. Rulmont, R. Cloots, B. Vertruyen, *J. Eur. Ceram. Soc.* 27 (2007) 3469–3474.

[49] J.A. Villoria, M.C. Alvarez-Galvan, S.M. Al-Zahrani, P. Palmisano, S. Specchia, V. Specchia, J.L.G. Fierro, R.M. Navarro, *Appl. Catal. B* 105 (2011) 276–288.

[50] D. Johnson, *Zview Program. Version 3.0*, Scribner Associates, Inc., Southern Pines, North Carolina, 1990–2007.

[51] C. Deportes, M. Duclot, P. Fabry, J. Fouletier, A. Hammou, M. Kleitz, E. Siebert, in: J.L. Souquet (Ed.), *Electrochimie des Solides*, PUG, 2004, p. 305.

[52] E. Lay, L. Dessemond, G. Gauthier, *J. Power Sources* 221 (2013) 149–156.

[53] S.B. Ha, P.S. Cho, Y.H. Cho, D. Lee, J.H. Lee, *J. Power Sources* 195 (2010) 124–129.

[54] S.P. Jiang, L. Zhang, C.S. Cheng, Y. Zhang, *ECS Trans.* 7 (1) (2007) 1081–1088.

[55] L. Zhang, S.P. Jiang, C.S. Cheng, Y. Zhang, *J. Electrochem. Soc.* 154 (6) (2007) B577–B582.

[56] L. Deleebeeck, J.L. Fournier, V. Birss, *Solid State Ionics* 181 (2010) 1229–1237.

[57] E. Lay, G. Gauthier, L. Dessemond, *Solid State Ionics* 189 (2011) 91–99.

[58] M. Al Daroukh, V.V. Vashook, H. Ullmann, F. Tietz, I. Arual Raj, *Solid State Ionics* 158 (2003) 141–150.

[59] J.H. Kuo, H.U. Anderson, D.M. Sparlin, *J. Solid State Chem.* 83 (1989) 52–60.

[60] T. Ishihira, S. Fukui, M. Enoki, H. Matsumoto, *J. Electrochem. Soc.* 153 (2006) A2085–A2090.

[61] F.C. Fonseca, E.N.S. Muccillo, R. Muccillo, D.Z. de Florio, *J. Electrochem. Soc.* 155 (5) (2008) B483–B487.

[62] M. van den Bossche, S. McIntosh, *Chem. Mater.* 22 (2010) 5856–5865.